Transcriptional reprogramming from innate immune functions to a pro-thrombotic signature upon SARS-CoV-2 sensing by monocytes in COVID-19.

Allison K. Maher[1], Katie L. Burnham[2], Emma Jones[1], Laury Baillon[1], Claudia Selck[1], Nicolas Giang[1], Rafael Argüello[3], Charlotte-Eve Short[1], Rachael Quinlan[1], Wendy S. Barclay[1], Nichola Cooper[4], Graham P. Taylor[1], Emma E. Davenport[2], Margarita Dominguez-Villar[1],*.

Affiliations

1 Department of Infectious Diseases, Faculty of Medicine, Imperial College London, London, UK.
2 Wellcome Sanger Institute, Wellcome Genome Campus, Hinxton, Cambridge, UK.
3 Aix Marseille Université, CNRS, INSERM, CIML, Centre d'Immunologie de Marseille-Luminy, Marseille, France.
4 Department of Immunology and Inflammation, Faculty of Medicine, Imperial College London, UK.
* correspondence to m.dominguez-villar@imperial.ac.uk

Abstract
Alterations in the myeloid immune compartment have been observed in COVID-19, but the specific mechanisms underlying these impairments are not completely understood. Here we examined the functionality of classical CD14+ monocytes as a main myeloid cell component in well-defined cohorts of patients with mild and moderate COVID-19 during the acute phase of infection and compared them to that of healthy individuals. We found that *ex vivo* isolated CD14+ monocytes from mild and moderate COVID-19 patients display specific patterns of costimulatory and inhibitory receptors that clearly distinguish them from healthy monocytes, as well as altered expression of histone marks and a dysfunctional metabolic profile. Decreased NFκB activation in COVID-19 monocytes *ex vivo* is accompanied by an intact type I IFN antiviral response. Subsequent pathogen sensing *ex vivo* led to a state of functional unresponsiveness characterized by a defect in pro-inflammatory cytokine expression, NFκB-driven cytokine responses and defective type I IFN response in moderate COVID-19 monocytes. Transcriptionally, COVID-19 monocytes switched their gene expression signature from canonical innate immune functions to a pro-thrombotic phenotype characterized by increased expression of pathways involved in hemostasis and immunothrombosis. In response to SARS-CoV-2 or other viral or bacterial components, monocytes displayed defects in the epigenetic remodelling and metabolic reprogramming that usually occurs upon pathogen sensing in innate immune cells. These results provide a potential mechanism by which innate immune dysfunction in COVID-19 may contribute to disease pathology.

Main text

COVID-19 is a respiratory tract infection caused by severe acute respiratory syndrome corona virus 2 (SARS-CoV-2). In unvaccinated individuals, the majority of infections are mild or asymptomatic, but 15% of patients develop moderate to severe disease requiring hospitalisation,

and 5% develop critical disease with life-threatening pneumonia, acute respiratory distress syndrome (ARDs) and septic shock[1]. During the acute phase of infection, myeloid cells including monocytes and macrophages are the most enriched immune cell types in the lungs of COVID-19 patients and play a major role in the pathogenicity of the disease[2,3]. Moreover, contrasting observations regarding the development of cytokine storms vs. immunosuppression[4,5] and the overactive or deficient type I IFN response in the lungs and in peripheral blood[6-11] have been described for the role of myeloid cells in COVID-19[12]. Despite these apparent contrasting works, most studies have observed dysregulated innate immune responses and reduced expression of human leukocyte antigen DR isotype (HLA-DR) by circulating myeloid cells, which is considered a marker of immune suppression[10,13-17].

Monocytes are blood-circulating, phagocytic, innate immune leukocytes with important functions in pathogen sensing, and innate and adaptive immune response activation during viral infection[18]. Despite their heterogeneity[19], monocytes are broadly classified into three subsets based on the expression of CD14 and CD16 into classical ($CD14^+CD16^-$), intermediate ($CD14^+CD16^+$), and nonclassical ($CD14^{low}CD16^+$) monocytes[18]. During viral infection, circulating monocytes infiltrate affected tissues and differentiate into inflammatory macrophages and dendritic cells (DCs)[20], contributing to pathogen clearance and tissue regeneration.

Here we deeply examined the phenotype and functionality of the main monocyte population in humans, i.e. classical $CD14^+$ monocytes, in patients with COVID-19 and compared them to those of healthy individuals. We found that *ex vivo* isolated $CD14^+$ monocytes from mild and moderate COVID-19 patients are phenotypically different from monocytes from healthy individuals, displaying differential expression of costimulatory receptors and MHC molecules, epigenetic alterations and a dysfunctional metabolic profile that is accompanied by decreased *ex vivo* NFκB activation, while maintaining an intact type I IFN antiviral response. Subsequent pathogen sensing *ex vivo* led to a state of functional unresponsiveness that correlated transcriptionally with that of a endotoxin-induced tolerance signature. Moreover, monocytes switched their gene expression signature from canonical innate immune functions to a pro-thrombotic phenotype characterized by increased expression of pathways involved in immunothrombosis. In response to SARS-CoV-2 or other viral or bacterial components, monocytes displayed decreased expression of type I IFN responses, decreased pro-inflammatory cytokine production and costimulatory receptor expression and defects in the epigenetic remodelling and metabolic reprogramming that usually occurs upon pathogen sensing. These results provide a potential mechanism by which innate immune dysfunction in COVID-19 contributes to disease progression and identifies potential therapeutic targets.

Phenotypic and epigenetic alterations in COVID-19 monocytes.

Global alterations in innate immune cell phenotypes have been identified in severe COVID-19[11,21-23]. As the main human monocyte population, we focused on deeply characterizing the *ex vivo* phenotype of classical $CD14^+$ monocytes in uninfected healthy individuals and patients with COVID-19 presenting with mild or moderate symptoms (1-2 or 3-4 WHO ordinal scale for COVID-19 severity, respectively) during the acute phase of disease. The battery of markers examined by high dimensional flow cytometry included MHC molecules and costimulatory and

2

93   coinhibitory receptors (Figure 1). Dimensionality reduction tools demonstrated that while some
94   overlap in the global phenotypes was observed among the three study groups, monocytes from
95   healthy individuals were clearly distinct from both mild and moderate COVID-19 on a tSNE plot
96   (Figure 1a). In addition, COVID-19 monocytes could also be distinguished based on disease
97   severity, with main cell clusters for both disease severity groups mapping separately on the tSNE
98   plots. Moderate COVID-19 monocytes expressed decreased levels of HLA-DR, in agreement with
99   previous reports[10,17], but in contrast, they displayed increased expression of HLA-ABC compared
100   to both mild disease and uninfected individuals, suggesting a skewed trend towards class I antigen
101   presentation (Figure 1b). In addition, moderate COVID-19 monocytes expressed increased levels
102   of the c-type lectin CD301. The decreased expression of the costimulatory receptor CD86 and
103   increased expression of the inhibitory receptors TIM-3[24] and PD-1[25] on moderate COVID-19
104   monocytes suggest an altered activation profile skewed towards an inhibitory phenotype.
105   Furthermore, there were significant differences in the expression of certain markers on mild vs.
106   moderate COVID-19 monocytes. For example, downregulation of HLA-DR and CD86 and
107   upregulation of TIM-3 and HLA-ABC compared to healthy monocytes were only significant in
108   moderate but not on mild COVID-19 monocytes, and the increased expression of CD80 in mild
109   COVID-19 compared to healthy monocytes was not apparent in moderate COVID-19. These
110   results suggest a more profound dysfunction in moderate than in mild COVID-19 monocytes.
111
112   To further define and quantify the phenotypic differences observed between healthy individuals
113   and COVID-19 patients, we applied clustering algorithms using the 12 phenotypic markers
114   previously examined. Cell clustering identified 16 different subpopulations of monocytes that were
115   distinctively distributed in healthy and COVID-19 monocytes (Figure 1c, d), with 11 clusters
116   containing more than 88% of the total cells analyzed (Supplementary Figure 1). Interestingly,
117   expansion of specific monocyte subpopulations were different in mild and moderate COVID-19
118   monocytes, and while mild monocytes, in contrast to healthy monocytes, predominantly contained
119   clusters 1, 3 and 4 and did not contain clusters 2 and 5, monocytes from moderate COVID-19
120   patients significantly had reduced frequency of cells from clusters 1, 3 and 4, and contained
121   expanded clusters 6 and 8 (Figure 1d and Supplementary Table 2). As a consequence, the
122   distribution of cells from healthy, mild and moderate COVID-19 monocytes was clearly different
123   in each cluster, and while some cell clusters were composed of cells from all disease groups, such
124   as clusters 10, 11 and 13, other clusters predominantly contained cells from one or two particular
125   disease groups. For example, clusters 1, 3, 4, 12 and 16 were predominantly composed of cells
126   from mild patients, while clusters 6 and 8 predominantly contained moderate COVID-19
127   monocytes and were almost absent in monocytes from healthy individuals (Figure 1e). Normalized
128   expression levels of the markers defining each cluster demonstrated that the phenotype of cluster
129   6 was mostly driven by downregulation of CD86 and HLA-DR, while that of cluster 8 was mostly
130   driven by the increased expression of HLA-ABC (Figure 1f). Collectively, these results reveal that
131   distinct populations of circulating monocytes are enriched in mild and moderate COVID-19
132   patients.
133
134
135   As a measurement of global differences in the patterns of activation/repression of gene expression
136   we looked at the protein expression of histone marks associated with active gene transcription
137   (H3K27Ac and H3K4Me3[26,27], Figure 1g) and gene repression (H3K9Me2 and H3K27Me3[26,27],
138   Figure 1h) in monocytes from healthy individuals and patients with COVID-19 *ex vivo*. Significant

139   differences in the expression of epigenetic marks associated with activation of gene expression
140   were found. Monocytes from mild COVID-19 patients displayed increased levels of both
141   H3K27Ac and H3K4Me3 compared to healthy individuals as expected considering the *in vivo*
142   pathogen sensing and subsequent activation of innate immunity by an ongoing viral infection[28].
143   However, moderate COVID-19 monocytes failed to increase H3K27Ac and H3K4Me3 expression
144   and displayed similar levels to those of healthy individuals (Figure 1g). Moreover, while no
145   differences were observed in the expression of the repressive mark H3K9Me2, the increased
146   H3K27Me3 observed in mild COVID-19 monocytes was not observed in moderate COVID-19.
147   These results suggest that the epigenetic remodeling associated with virus sensing and subsequent
148   activation of innate immunity is defective in moderate COVID-19 monocytes.

150   ***Ex vivo* RNA-seq uncovers metabolic dysfunction in moderate COVID-19 monocytes.**

152   The fundamental differences in the phenotype and epigenetic marks in moderate COVID-19
153   monocytes compared to those of healthy individuals led us to investigate in depth the gene
154   expression profile of *ex vivo* isolated classical CD14$^+$ monocytes from patients with moderate
155   COVID-19 and compare them with those of healthy individuals (Figure 2). Principal component
156   analysis (PCA) applied to examine the global distribution of gene expression profiles from
157   COVID-19 monocytes (n=10) and healthy individuals (n=6) demonstrated a clear separation
158   between groups along PC1 (Figure 2a), with genes encoding a number of soluble factors,
159   chemokines and class II molecules as the main genes contributing to the separation between
160   healthy and COVID-19 monocytes (Supplementary Figure 2). Differential gene expression
161   analysis yielded 422 upregulated and 187 downregulated genes (≥1.5-fold change, FDR<0.05) in
162   COVID-19 monocytes compared to healthy controls (Figure 2b). We used these genes to perform
163   a pathway enrichment analysis with XGR[29] and pathway annotations from Reactome to gain
164   insight on potential pathways differentially expressed in COVID-19 monocytes (Supplementary
165   Figure 3). Interestingly, pathway enrichment identified glycolysis as the most enriched pathway
166   in COVID-19 monocytes together with metabolism of lipids and lipoproteins. Moreover, the
167   presence of interferon signaling and cytokine signaling in the list of enriched pathways was in
168   agreement with previous reports on the role of these two pathways in COVID-19 pathogenesis[6,17,23]
169   (Supplementary Figure 3 and Supplementary Table 3).

171   We subsequently examined the directionality of expression of the enriched pathways by analyzing
172   downregulated genes and upregulated genes separately. Pathway enrichment analysis of genes
173   significantly upregulated (≥1.5-fold change, FDR<0.05) in COVID-19 compared to healthy
174   individuals demonstrated a significant increase in the metabolism of a number of lipids, including
175   sphingolipids, phospholipids and lipoproteins. Other upregulated pathways in COVID-19
176   monocytes included interferon signaling, cytokine signaling and transmembrane transport of small
177   molecules. Heatmap showing the top 40 upregulated genes from the enriched pathways
178   demonstrated a somewhat variable expression patterns among COVID-19 monocytes and included
179   a number of type I interferon-stimulated genes (*IFI27*, *IFITM2*, *IFI6*, *IFITM3*, *MX1*), metabolic
180   enzymes (*ASAH1*, *CYP27A1*, *SGPP2*, *SPHK1*) and others (Figure 2d). Interestingly, the highest
181   expressed IFN-related gene was *IFI27*, which has been suggested as a biomarker of early SARS-
182   CoV-2 infection[30]. The increased type I IFN gene signature in COVID-19 monocytes was
183   confirmed by the increased *ex vivo* phospho-IRF3 protein expression in moderate COVID-19
184   patients compared to healthy individuals (Figure 2e) and by the increased expression of *IFITM2*

185   as an IFN-stimulated gene, measured by real-time PCR in an expanded cohort of mild and
186   moderate COVID-19 patients (Figure 2f). NFκB activation was examined *ex vivo* indirectly by
187   IκBα expression and directly by phosphorylation of the p65 NFκB subunit, as a readout for
188   cytokine signaling[31,32]. While mild, unlike moderate COVID-19 monocytes displayed a decrease
189   in the expression of IκBα compared to that of healthy individual monocytes, neither mild or
190   moderate COVID-19 monocytes displayed an increased expression of phospho-p65 NFκB,
191   suggesting that other additional mechanisms may be regulating the activation of NFκB, and that
192   NFκB-driven cytokine responses may be altered in patients with COVID-19, in agreement with
193   the lack of increased pro-inflammatory cytokine expression by COVID-19 monocytes (Figure 2c)
194   and with previous single cell transcriptomic data of acute COVID-19 PBMC[33]. Moreover, several
195   of the genes contributing to the "Cytokine signaling" pathway enrichment (Figure 2c) were
196   interferon-stimulated genes (Supplementary Table 4).

198   We subsequently selected the set of significantly downregulated genes (≥1.5 fold decrease,
199   FDR<0.05) in COVID-19 monocytes to perform pathway enrichment. The only pathway that was
200   significantly downregulated in COVID-19 monocytes was glycolysis (Figure 2h, I and
201   Supplementary Table 5). This metabolic profile with increased metabolism of lipids (Figure 2c)
202   and decreased glycolysis was unexpected, as glycolysis is an important driver of innate immune
203   cell function during the recognition of pathogens[34]. We used SCENITH[TM35] to metabolically
204   profile CD14^{+} monocytes from COVID-19 patients and healthy controls *ex vivo*. SCENITH[TM] uses
205   protein synthesis as a measurement of global metabolic activity. Puromycin incorporation is used
206   as a reliable readout of protein synthesis levels (and therefore metabolic activity) *in vitro* and *in*
207   *vivo*. In agreement with the pathway enrichment results, *ex vivo* puromycin incorporation was
208   significantly decreased in moderate COVID-19 monocytes (Figure 2j) compared to healthy
209   individuals, suggesting decreased metabolic activity. Moreover, the glycolytic capacity of
210   COVID-19 monocytes was significantly decreased in moderate patients and correlated with
211   disease severity (Figure 2k), and this was accompanied by a concomitant increase in metabolic
212   dependency in monocytes from moderate COVID-19 patients. The decreased metabolic activity
213   and glycolytic capacity was further confirmed by Seahorse analysis of extracellular acidification
214   rate and oxygen consumption rate as readouts for glycolysis and oxidative phosphorylation,
215   respectively (Supplementary Figure 4).

217   These data suggest that monocytes from COVID-19 patients with moderate disease display
218   epigenetic alterations and a dysfunctional metabolic profile that is accompanied by decreased
219   NFκB activation, while maintaining intact type I IFN antiviral responses.

221   **COVID-19 monocytes display impaired pathogen sensing and activation mechanisms *ex vivo*.**

223   The dysfunctional metabolic profile with a downregulation of glycolysis and the defective
224   activation of NFκB, both pathways heavily involved in the activation of innate immune cells upon
225   virus encounter[32,34], led us to examine the functional capacity of monocytes to sense and respond
226   to SARS-CoV2 *ex vivo* (Figure 3). Stimulation of CD14^{+} monocytes from healthy individuals with
227   SARS-CoV-2 led to a significant increase in both TNF and IL-10 production (Figure 3a).
228   However, COVID-19 monocytes significantly produced less TNF as compared to healthy
229   monocytes, while no differences were observed in IL-10 expression (Figure 3b). Moreover, the
230   defect in TNF production upon stimulation was not SARS-CoV-2-specific, as stimulation with

231 common cold coronaviruses or bacterial lipopolysaccharide (LPS) also led to significantly reduced
232 TNF production compared to monocytes from healthy individuals (Figure 3c). In addition, the
233 expression of CD40 (Figure 3d), which is important for monocyte effector function and is
234 upregulated after virus sensing[36], was increased in monocytes from healthy individuals but not on
235 COVID-19 monocytes (Figure 3e). This decreased expression was confirmed after stimulation
236 with common cold coronaviruses or LPS (Figure 3f), suggesting that the activation defects in
237 COVID-19 monocytes in response to pathogen sensing were not specific to SARS-CoV-2. In
238 addition to CD40, we also examined the expression of other cell surface receptors involved in
239 antigen presentation and activation of T cells. (Figure 3g) HLA-DR expression levels were not
240 further upregulated upon SARS-CoV-2 stimulation in any of the patient groups, and stimulation
241 still maintained the differences in expression observed *ex vivo* among groups (Figure 1b).
242 Moreover, while CD80 was significantly upregulated in healthy, mild and moderate COVID-19
243 monocytes after SARS-CoV-2 stimulation, only healthy monocytes increased the expression of
244 CD86 after stimulation (Figure 3g).

246 Epigenetic reprogramming underlies innate immune cell activation upon pathogen sensing. In
247 agreement with this, monocytes from healthy individuals significantly increased the expression of
248 H3K27Ac and H3K4Me3, associated with activation of gene expression[26,27], upon SARS-CoV-2
249 stimulation. In contrast, monocytes from moderate COVID-19 patients did not change the
250 expression of these histone marks after SARS-CoV-2 sensing. Monocytes from mild COVID-19
251 patients demonstrated an intermediate pattern of expression, with significant upregulation of
252 H3K27Ac but no change in H3K4Me3 upon SARS-CoV-2 stimulation (Figure 3h). Moreover,
253 mild patient monocytes significantly decreased the expression of repressive H3K27Me3 and
254 H3K9Me2 marks, while neither healthy or moderate COVID-19 monocytes did after stimulation
255 with SARS-CoV-2 (Figure 3i).

257 The apparent unresponsiveness of COVID-19 monocytes to pathogen sensing was accompanied
258 by altered metabolic reprogramming. Innate immune cells that sense pathogens increase the rate
259 of glycolysis over mitochondrial oxidative phosphorylation to enable fast energy availability [37-39].
260 However, COVID-19 monocyte energetic profile measured by SCENITH[TM] did not increase upon
261 LPS stimulation, unlike that of healthy monocytes (Figure 3j). Moreover, moderate COVID-19
262 monocytes showed a decreased glycolytic capacity and an increase in fatty acid and amino acid
263 oxidation capacity (Figure 3k) compared to healthy monocytes, that correlated with a slight but
264 significant decrease in glucose dependency and an increase in mitochondrial dependency
265 compared to monocytes from healthy individuals (Supplementary Figure 5). These data are in
266 agreement with the enriched metabolic pathways from RNA-seq data (Figures 2c and 2h).
267 Seahorse experiments confirmed the defect in glycolysis in stimulated monocytes from COVID-
268 19 patients (Supplementary Figure 6). In summary, monocytes from COVID-19 patients display a
269 profound defect in pathogen sensing *ex vivo* that is more evident in moderate than in mild patients
270 and is characterized by an impairment in pro-inflammatory cytokine production and expression of
271 activation-related receptors, epigenetic reprogramming and metabolic rewiring.

273 **SARS-CoV-2-stimulated monocytes from COVID-19 patients display a pro-thrombotic gene**
274 **expression signature.**

6

276 To globally characterize the gene expression signature of activated monocytes in COVID-19, we
277 performed RNA-seq on SARS-CoV-2-stimulated monocytes from healthy individuals and patients
278 with moderate COVID-19 (Figure 4). PCA clearly separated COVID-19 from healthy monocytes,
279 although some healthy monocytes clustered with COVID-19 in the principal component space
280 (Figure 4a, Supplementary Figure 7). Quantification of differentially expressed genes yielded
281 1,437 upregulated and 2,073 downregulated genes in activated COVID-19 compared to activated
282 healthy monocytes (≥1.5 fold change, FDR<0.05, Figure 4b). Pathway enrichment of differentially
283 expressed genes (≥1.5 fold change vs. healthy monocytes, FDR<0.05) using XGR software and
284 the Reactome pathway database demonstrated a number of expected pathways involved in the
285 innate immune response to pathogens, including type I IFN signaling, cytokine signaling,
286 interactions between lymphoid and non-lymphoid cells, NLR sensing, etc (Supplementary Figure
287 8 and Supplementary Table 6). However, when we focused our analysis on pathways enriched in
288 upregulated genes in activated COVID-19 monocytes compared to activated healthy monocytes,
289 the most significantly enriched pathways were involved in hemostasis and coagulation, including
290 integrin signaling, extracellular matrix organization, signaling by PDGF, interactions with
291 activated platelets and general hemostasis (Figure 4c and Supplementary Table 7). Integrin
292 receptors are used by cells to interact with other cells and with the extracellular matrix, by binding
293 numerous matrix proteins including collagen, actin and laminin being also involved in hemostasis
294 and platelet aggregation[40]. In addition, monocytes actively bind to platelets forming pro-
295 thrombotic aggregates in inflammatory and vascular pathologies[41,42]. Monocytes from COVID-19
296 patients expressed increased levels of various collagen subunits (*COL1A1*, *PLOD2*, *COL6A3*,
297 *COL6A1*), enzymes involved in collagen triple helix synthesis (*COLGALT1*) and a number of
298 matrix metalloproteinases (*MMP1*, *MMP2*, *MMP14*, Figure 4d), which are not only involved in
299 extracellular matrix remodeling, but they have also been implicated in contributing directly to
300 platelet activation and priming for aggregation[43,44]. These results are in agreement with the clinical
301 observations of hypercoagulability and acquired coagulopathies in patients with COVID-19[45-48],
302 and suggest that monocytes from moderate COVID-19 patients upregulate a pro-thrombotic gene
303 expression signature upon further SARS-CoV-2 sensing.
304
305 Interestingly, downregulated pathways in stimulated COVID-19 monocytes included most of the
306 canonical immunological functions expected for innate immune cells upon virus sensing, i.e.
307 interferon signaling, RIG-I/MDA5-mediated induction of interferons, activation of TCR signaling
308 in T cells, innate immune functions and interactions with non-lymphoid cells (Figure 4e and
309 Supplementary Table 8). The majority of the top 40 genes significantly downregulated in COVID-
310 19 monocytes from these downregulated pathways consisted of different interferons (*IFNA1*,
311 *IFNA2*, *IFNA14* and *IFNB1*), interferon-stimulated genes (*IFIT3*, *ISG15*, *IFIT2*, *ISG20*, *IRF7* and
312 *MX2*) and pathogen-sensing receptors (*TLR7*, *AIM2*, Figure 4f). This gene signature was
313 functionally confirmed by examining the activation pattern of IRF3 in response to LPS in
314 monocytes from healthy individuals and patients with mild and moderate COVID-19 (Figure 4g).
315 While healthy and mild COVID-19 monocytes significantly increased the expression of the
316 phosphorylated form of IRF3 upon LPS stimulation compared to baseline levels, monocytes from
317 moderate patients did not. This inability to activate IRF3 correlated with decreased expression of
318 the interferon-stimulated gene *IFITM2*, examined in an expanded cohort of healthy, mild and
319 moderate COVID-19 monocytes after stimulation with SARS-CoV-2 (Figure 4h). Of note,
320 examination of NFκB p65 activation, as a main transcription factor involved in cytokine signaling

321 in innate cells, demonstrated a defective activation in both mild and moderate COVID-19 as
322 compared to healthy individuals (Figure 4i).
323
324 These findings are consistent with an unexpected transcriptional and functional switch of COVID-
325 19 monocytes from canonical innate immune functions to a pro-thrombotic phenotype and
326 potential cross-talk with other cells involved in hemostasis, which suggests that activated
327 monocytes may contribute to COVID-19 severity by actively impacting hemostasis and by a
328 reduction in innate immune functions necessary for efficient virus clearance.
329
330 **Endotoxin tolerance signature enriched in activated COVID-19 monocytes**.
331
332 A number of works have suggested similarities between the characteristics of the immune response
333 in COVID-19 patients and those of septic individuals, including multiple organ dysfunction,
334 immunosuppression, coagulopathies and acute respiratory failure[49]. To determine the similarities
335 between the transcriptional signature of COVID-19 monocytes with that of sepsis monocytes, we
336 utilized publicly available microarray gene expression data on sepsis monocytes and healthy
337 controls[50] and we tested the estimated fold changes for correlation with those from our *ex vivo*
338 (Figure 5a) and activated (Figure 5b) COVID-19 and healthy monocytes. No clear correlation was
339 observed in any of the two contrasts, which suggest that the transcriptional signature of CD14$^+$
340 monocytes in moderate COVID-19 is not similar to that of monocytes in sepsis.
341
342 The lack of cytokine expression, activation of costimulatory receptors, impaired antigen
343 presentation potential and metabolic impairments displayed by moderate COVID-19 monocytes
344 resembled the phenotype observed in LPS-induced tolerance[51]. We have previously defined an
345 endotoxin tolerance gene expression signature from publicly available microarray data on
346 monocytes stimulated *in vitro* with LPS[52] that comprises 398 genes. Out of these, 318 genes were
347 detected in our RNA-seq dataset. We tested for correlation of the endotoxin tolerance signature
348 with *ex vivo* (Figure 5c) and activated (Figure 5d) COVID-19 monocytes, and while *ex vivo*
349 COVID-19 monocytes did not display a clear correlation with the tolerance signature, activated
350 COVID-19 monocytes displayed similar directionality of expression in those genes from the
351 tolerance signature that were detected in the dataset. These data were further confirmed in barcode
352 plots (Figure 5e), showing a statistically significant enrichment of the endotoxin tolerance gene
353 signature in the list of differentially expressed genes from stimulated COVID-19 monocytes
354 compared to healthy controls, for both upregulated and downregulated genes.
355
356 **Discussion.**
357 Here we employed metabolic, transcriptomic and functional assays to identify a number of
358 phenotypic and functional alterations of COVID-19 monocytes that characterize moderate disease
359 and we have provided the functional characteristics of monocyte responses in mild SARS-CoV-2
360 infections as an example of an efficiently and successfully cleared infection without excessive
361 immunopathology. Important alterations in epigenetic marks, metabolism and transcriptional
362 signatures characterize moderate COVID-19 monocytes and are important aspects of a global
363 unresponsiveness phenotype upon pathogen sensing characterized by a transcriptional switch from
364 canonical innate immune functions to a pro-thrombotic signature. Epigenetic and metabolic
365 defects probably underlie the observed dysfunctional phenotype as they modulate innate immune
366 functions including cytokine expression, activation, phagocytic capacity, etc[34,53,54]. Moreover, it

367 would be plausible that these two mechanisms are interlinked. For example, the defects in histone
368 acetylation could be due to a lack of acetyl groups, which are mostly provided by acetyl-CoA
369 generated as a glycolysis product[55], which is inhibited in COVID-19 monocytes (Figures 2 and 3).
370

371 A question that remains to be answered is the driver(s) of the described circulating monocyte
372 dysfunction. *Ex vivo*, pathogen sensing triggers a switch in COVID-19 monocyte gene expression
373 signature from canonical innate immune functions to pro-thrombotic phenotype. It remains to be
374 determined whether other soluble factors in the microenvironment contribute to this
375 reprogramming, or even the direct infection of monocytes by SARS-CoV-2, which has been
376 previously suggested[56]. The phenotype we observed in circulating monocytes is in clear contrast
377 with the functionality of monocyte-derived macrophages in the lung of COVID19 patients[10]. In
378 this regard, our study is limited by the lack of bronchoalveolar lavage fluid (BALF) paired samples
379 to compare the phenotype and function of circulating monocytes with those infiltrating the target
380 tissue. However, some previous publications examining paired airway and blood samples have
381 shown differences in the signatures of circulating and lung innate immune cells, with low HLA-
382 DR expressing, dysfunctional monocytes in the blood and hyperactive airway monocyte and
383 macrophages producing pro-inflammatory cytokines[10,33,57]. The underlying mechanisms for these
384 differences remain elusive. During the course of viral infections, circulating monocytes rapidly
385 leave the bloodstream and migrate to target tissues, where after pathogen sensing and/or other
386 microenvironmental stimuli, they differentiate into macrophages and/or dendritic cells. In this
387 study we examined the functionality of monocytes during the acute phase of disease, early after
388 symptom onset. It remains to be determined whether these dysfunctional monocytes have the
389 capacity to migrate to the lungs and contribute to lung inflammation, or whether their dysfunction
390 is such that migration is impaired and monocyte migration only occurred during the very initial
391 phases of infection before monocyte acquired the impairments observed in this study. Of note,
392 some of the defective pathways displayed by COVID-19 monocytes, as for example glycolysis,
393 have been shown to be essential for migration of other cells to target tissue[58,59]. Finally, the results
394 described in this study beg the question of whether the functional impairments observed in
395 monocytes during the acute phase of infection are COVID-19-specific. While stimulation with
396 other viruses and bacterial products led to similar altered immune phenotypes in COVID-19
397 monocytes (Figure 3), it seems likely that these processes occur with other moderate respiratory
398 viral infections, as is the case during seasonal Influenza vaccination[60]. Longitudinal studies of
399 monocyte dynamics during SARS-CoV-2 and other respiratory viral infections using both blood
400 and BALF samples are warranted to answer these questions.
401

402 **Main references**
403
404

405 1   Fu, L. *et al.* Clinical characteristics of coronavirus disease 2019 (COVID-19) in China: A
406   systematic review and meta-analysis. *J Infect* **80**, 656-665, doi:10.1016/j.jinf.2020.03.041
407   (2020).
408 2   Bost, P. *et al.* Host-Viral Infection Maps Reveal Signatures of Severe COVID-19 Patients.
409   *Cell* **181**, 1475-1488 e1412, doi:10.1016/j.cell.2020.05.006 (2020).
410 3   Merad, M. & Martin, J. C. Pathological inflammation in patients with COVID-19: a key
411   role for monocytes and macrophages. *Nat Rev Immunol* **20**, 355-362, doi:10.1038/s41577-
412   020-0331-4 (2020).

413 4 Jafarzadeh, A., Chauhan, P., Saha, B., Jafarzadeh, S. & Nemati, M. Contribution of
414 monocytes and macrophages to the local tissue inflammation and cytokine storm in
415 COVID-19: Lessons from SARS and MERS, and potential therapeutic interventions. *Life
416 Sci* **257**, 118102, doi:10.1016/j.lfs.2020.118102 (2020).
417 5 Remy, K. E. *et al.* Severe immunosuppression and not a cytokine storm characterizes
418 COVID-19 infections. *JCI Insight* **5**, doi:10.1172/jci.insight.140329 (2020).
419 6 Hadjadj, J. *et al.* Impaired type I interferon activity and inflammatory responses in severe
420 COVID-19 patients. *Science* **369**, 718-724, doi:10.1126/science.abc6027 (2020).
421 7 Lee, J. S. & Shin, E. C. The type I interferon response in COVID-19: implications for
422 treatment. *Nat Rev Immunol* **20**, 585-586, doi:10.1038/s41577-020-00429-3 (2020).
423 8 Ramasamy, S. & Subbian, S. Critical Determinants of Cytokine Storm and Type I
424 Interferon Response in COVID-19 Pathogenesis. *Clin Microbiol Rev* **34**,
425 doi:10.1128/CMR.00299-20 (2021).
426 9 Zhang, J., Zhao, C. & Zhao, W. Virus Caused Imbalance of Type I IFN Responses and
427 Inflammation in COVID-19. *Frontiers in Immunology* **12**,
428 doi:10.3389/fimmu.2021.633769 (2021).
429 10 Liao, M. *et al.* Single-cell landscape of bronchoalveolar immune cells in patients with
430 COVID-19. *Nat Med* **26**, 842-844, doi:10.1038/s41591-020-0901-9 (2020).
431 11 Schulte-Schrepping, J. *et al.* Severe COVID-19 Is Marked by a Dysregulated Myeloid Cell
432 Compartment. *Cell* **182**, 1419-1440 e1423, doi:10.1016/j.cell.2020.08.001 (2020).
433 12 McKechnie, J. L. & Blish, C. A. The Innate Immune System: Fighting on the Front Lines
434 or Fanning the Flames of COVID-19? *Cell Host Microbe* **27**, 863-869,
435 doi:10.1016/j.chom.2020.05.009 (2020).
436 13 Giamarellos-Bourboulis, E. J. *et al.* Complex Immune Dysregulation in COVID-19
437 Patients with Severe Respiratory Failure. *Cell Host Microbe* **27**, 992-1000 e1003,
438 doi:10.1016/j.chom.2020.04.009 (2020).
439 14 Payen, D. *et al.* A Longitudinal Study of Immune Cells in Severe COVID-19 Patients.
440 *Front Immunol* **11**, 580250, doi:10.3389/fimmu.2020.580250 (2020).
441 15 Silvin, A. *et al.* Elevated Calprotectin and Abnormal Myeloid Cell Subsets Discriminate
442 Severe from Mild COVID-19. *Cell* **182**, 1401-1418 e1418, doi:10.1016/j.cell.2020.08.002
443 (2020).
444 16 Spinetti, T. *et al.* Reduced Monocytic Human Leukocyte Antigen-DR Expression Indicates
445 Immunosuppression in Critically Ill COVID-19 Patients. *Anesth Analg* **131**, 993-999,
446 doi:10.1213/ANE.0000000000005044 (2020).
447 17 Lucas, C. *et al.* Longitudinal analyses reveal immunological misfiring in severe COVID-
448 19. *Nature* **584**, 463-469, doi:10.1038/s41586-020-2588-y (2020).
449 18 Kapellos, T. S. *et al.* Human Monocyte Subsets and Phenotypes in Major Chronic
450 Inflammatory Diseases. *Front Immunol* **10**, 2035, doi:10.3389/fimmu.2019.02035 (2019).
451 19 Villani, A. C. *et al.* Single-cell RNA-seq reveals new types of human blood dendritic cells,
452 monocytes, and progenitors. *Science* **356**, doi:10.1126/science.aah4573 (2017).
453 20 Serbina, N. V., Jia, T., Hohl, T. M. & Pamer, E. G. Monocyte-mediated defense against
454 microbial pathogens. *Annu Rev Immunol* **26**, 421-452,
455 doi:10.1146/annurev.immunol.26.021607.090326 (2008).
456 21 Saichi, M. *et al.* Single-cell RNA sequencing of blood antigen-presenting cells in severe
457 COVID-19 reveals multi-process defects in antiviral immunity. *Nat Cell Biol* **23**, 538-551,
458 doi:10.1038/s41556-021-00681-2 (2021).

459 22 Zhou, R. *et al.* Acute SARS-CoV-2 Infection Impairs Dendritic Cell and T Cell Responses.
460 *Immunity* **53**, 864-877 e865, doi:10.1016/j.immuni.2020.07.026 (2020).
461 23 Arunachalam, P. S. *et al.* Systems biological assessment of immunity to mild versus severe
462 COVID-19 infection in humans. *Science* **369**, 1210-1220, doi:10.1126/science.abc6261
463 (2020).
464 24 Zhang, Y. *et al.* Tim-3 regulates pro- and anti-inflammatory cytokine expression in human
465 CD14+ monocytes. *J Leukoc Biol* **91**, 189-196, doi:10.1189/jlb.1010591 (2012).
466 25 Pagliano, O. *et al.* Tim-3 mediates T cell trogocytosis to limit antitumor immunity. *J Clin*
467 *Invest*, doi:10.1172/JCI152864 (2022).
468 26 Kimura, H. Histone modifications for human epigenome analysis. *J Hum Genet* **58**, 439-
469 445, doi:10.1038/jhg.2013.66 (2013).
470 27 Shahbazian, M. D. & Grunstein, M. Functions of site-specific histone acetylation and
471 deacetylation. *Annu Rev Biochem* **76**, 75-100,
472 doi:10.1146/annurev.biochem.76.052705.162114 (2007).
473 28 Hoeksema, M. A. & de Winther, M. P. Epigenetic Regulation of Monocyte and
474 Macrophage Function. *Antioxid Redox Signal* **25**, 758-774, doi:10.1089/ars.2016.6695
475 (2016).
476 29 Fang, H., Knezevic, B., Burnham, K. L. & Knight, J. C. XGR software for enhanced
477 interpretation of genomic summary data, illustrated by application to immunological traits.
478 *Genome Med* **8**, 129, doi:10.1186/s13073-016-0384-y (2016).
479 30 Gupta, R. K. *et al.* Blood transcriptional biomarkers of acute viral infection for detection
480 of pre-symptomatic SARS-CoV-2 infection: a nested, case-control diagnostic accuracy
481 study. *Lancet Microbe* **2**, e508-e517, doi:10.1016/S2666-5247(21)00146-4 (2021).
482 31 de Marcken, M., Dhaliwal, K., Danielsen, A. C., Gautron, A. S. & Dominguez-Villar, M.
483 TLR7 and TLR8 activate distinct pathways in monocytes during RNA virus infection. *Sci*
484 *Signal* **12**, doi:10.1126/scisignal.aaw1347 (2019).
485 32 Liu, T., Zhang, L., Joo, D. & Sun, S. C. NF-kappaB signaling in inflammation. *Signal*
486 *Transduct Target Ther* **2**, doi:10.1038/sigtrans.2017.23 (2017).
487 33 Wilk, A. J. *et al.* A single-cell atlas of the peripheral immune response in patients with
488 severe COVID-19. *Nat Med* **26**, 1070-1076, doi:10.1038/s41591-020-0944-y (2020).
489 34 Kelly, B. & O'Neill, L. A. Metabolic reprogramming in macrophages and dendritic cells in
490 innate immunity. *Cell Res* **25**, 771-784, doi:10.1038/cr.2015.68 (2015).
491 35 Arguello, R. J. *et al.* SCENITH: A Flow Cytometry-Based Method to Functionally Profile
492 Energy Metabolism with Single-Cell Resolution. *Cell Metab* **32**, 1063-1075 e1067,
493 doi:10.1016/j.cmet.2020.11.007 (2020).
494 36 Kuroiwa, T. *et al.* CD40 ligand-activated human monocytes amplify glomerular
495 inflammatory responses through soluble and cell-to-cell contact-dependent mechanisms. *J*
496 *Immunol* **163**, 2168-2175 (1999).
497 37 Dominguez-Andres, J. *et al.* Rewiring monocyte glucose metabolism via C-type lectin
498 signaling protects against disseminated candidiasis. *PLoS Pathog* **13**, e1006632,
499 doi:10.1371/journal.ppat.1006632 (2017).
500 38 Lachmandas, E. *et al.* Microbial stimulation of different Toll-like receptor signalling
501 pathways induces diverse metabolic programmes in human monocytes. *Nat Microbiol* **2**,
502 16246, doi:10.1038/nmicrobiol.2016.246 (2016).
503 39 Schmidl, C. *et al.* Transcription and enhancer profiling in human monocyte subsets. *Blood*
504 **123**, e90-99, doi:10.1182/blood-2013-02-484188 (2014).

40   Nolte, M. A. & Margadant, C. Activation and suppression of hematopoietic integrins in hemostasis and immunity. *Blood* **135**, 7-16, doi:10.1182/blood.2019003336 (2020).

41   Mollnau, H. *et al.* Mechanisms of increased vascular superoxide production in an experimental model of idiopathic dilated cardiomyopathy. *Arterioscler Thromb Vasc Biol* **25**, 2554-2559, doi:10.1161/01.ATV.0000190673.41925.9B (2005).

42   Shantsila, E. & Lip, G. Y. The role of monocytes in thrombotic disorders. Insights from tissue factor, monocyte-platelet aggregates and novel mechanisms. *Thromb Haemost* **102**, 916-924, doi:10.1160/TH09-01-0023 (2009).

43   Galt, S. W. *et al.* Outside-in signals delivered by matrix metalloproteinase-1 regulate platelet function. *Circ Res* **90**, 1093-1099, doi:10.1161/01.res.0000019241.12929.eb (2002).

44   Versteeg, H. H., Heemskerk, J. W., Levi, M. & Reitsma, P. H. New fundamentals in hemostasis. *Physiol Rev* **93**, 327-358, doi:10.1152/physrev.00016.2011 (2013).

45   Al-Samkari, H. *et al.* COVID-19 and coagulation: bleeding and thrombotic manifestations of SARS-CoV-2 infection. *Blood* **136**, 489-500, doi:10.1182/blood.2020006520 (2020).

46   Middeldorp, S. *et al.* Incidence of venous thromboembolism in hospitalized patients with COVID-19. *J Thromb Haemost* **18**, 1995-2002, doi:10.1111/jth.14888 (2020).

47   Klok, F. A. *et al.* Incidence of thrombotic complications in critically ill ICU patients with COVID-19. *Thromb Res* **191**, 145-147, doi:10.1016/j.thromres.2020.04.013 (2020).

48   Rosen, R. J. Early thromboembolic events in hospitalized COVID-19 patients. *Thromb Res* **192**, 1, doi:10.1016/j.thromres.2020.05.004 (2020).

49   Olwal, C. O. *et al.* Parallels in Sepsis and COVID-19 Conditions: Implications for Managing Severe COVID-19. *Front Immunol* **12**, 602848, doi:10.3389/fimmu.2021.602848 (2021).

50   Shalova, I. N. *et al.* Human monocytes undergo functional re-programming during sepsis mediated by hypoxia-inducible factor-1alpha. *Immunity* **42**, 484-498, doi:10.1016/j.immuni.2015.02.001 (2015).

51   Wolk, K., Docke, W. D., von Baehr, V., Volk, H. D. & Sabat, R. Impaired antigen presentation by human monocytes during endotoxin tolerance. *Blood* **96**, 218-223 (2000).

52   del Fresno, C. *et al.* Potent phagocytic activity with impaired antigen presentation identifying lipopolysaccharide-tolerant human monocytes: demonstration in isolated monocytes from cystic fibrosis patients. *J Immunol* **182**, 6494-6507, doi:10.4049/jimmunol.0803350 (2009).

53   Mehta, S. & Jeffrey, K. L. Beyond receptors and signaling: epigenetic factors in the regulation of innate immunity. *Immunol Cell Biol* **93**, 233-244, doi:10.1038/icb.2014.101 (2015).

54   Jha, A. K. *et al.* Network integration of parallel metabolic and transcriptional data reveals metabolic modules that regulate macrophage polarization. *Immunity* **42**, 419-430, doi:10.1016/j.immuni.2015.02.005 (2015).

55   Yu, X., Ma, R., Wu, Y., Zhai, Y. & Li, S. Reciprocal Regulation of Metabolic Reprogramming and Epigenetic Modifications in Cancer. *Front Genet* **9**, 394, doi:10.3389/fgene.2018.00394 (2018).

56   Junqueira, C. *et al.* SARS-CoV-2 infects blood monocytes to activate NLRP3 and AIM2 inflammasomes, pyroptosis and cytokine release. *Res Sq*, doi:10.21203/rs.3.rs-153628/v1 (2021).

57   Szabo, P. A. *et al.* Longitudinal profiling of respiratory and systemic immune responses reveals myeloid cell-driven lung inflammation in severe COVID-19. *Immunity* **54**, 797-814 e796, doi:10.1016/j.immuni.2021.03.005 (2021).

58   Kishore, M. *et al.* Regulatory T Cell Migration Is Dependent on Glucokinase-Mediated Glycolysis. *Immunity* **47**, 875-889 e810, doi:10.1016/j.immuni.2017.10.017 (2017).

59   Shiraishi, T. *et al.* Glycolysis is the primary bioenergetic pathway for cell motility and cytoskeletal remodeling in human prostate and breast cancer cells. *Oncotarget* **6**, 130-143, doi:10.18632/oncotarget.2766 (2015).

60   Wimmers, F. *et al.* The single-cell epigenomic and transcriptional landscape of immunity to influenza vaccination. *Cell* **184**, 3915-3935 e3921, doi:10.1016/j.cell.2021.05.039 (2021).

61   Vergis, N. *et al.* Multi-arm Trial of Inflammatory Signal Inhibitors (MATIS) for hospitalised patients with mild or moderate COVID-19 pneumonia: a structured summary of a study protocol for a randomised controlled trial. *Trials* **22**, 270, doi:10.1186/s13063-021-05190-z (2021).

62   Levine, J. H. *et al.* Data-Driven Phenotypic Dissection of AML Reveals Progenitor-like Cells that Correlate with Prognosis. *Cell* **162**, 184-197, doi:10.1016/j.cell.2015.05.047 (2015).

63   Leibowitz, J., Kaufman, G. & Liu, P. Coronaviruses: propagation, quantification, storage, and construction of recombinant mouse hepatitis virus. *Curr Protoc Microbiol* **Chapter 15**, Unit 15E 11, doi:10.1002/9780471729259.mc15e01s21 (2011).

64   Dent, S. & Neuman, B. W. Purification of coronavirus virions for Cryo-EM and proteomic analysis. *Methods Mol Biol* **1282**, 99-108, doi:10.1007/978-1-4939-2438-7_10 (2015).

65   Kelley, J. L., Rozek, M. M., Suenram, C. A. & Schwartz, C. J. Activation of human blood monocytes by adherence to tissue culture plastic surfaces. *Exp Mol Pathol* **46**, 266-278, doi:10.1016/0014-4800(87)90049-9 (1987).

66   Dobin, A. *et al.* STAR: ultrafast universal RNA-seq aligner. *Bioinformatics* **29**, 15-21, doi:10.1093/bioinformatics/bts635 (2013).

67   Liao, Y., Smyth, G. K. & Shi, W. featureCounts: an efficient general purpose program for assigning sequence reads to genomic features. *Bioinformatics* **30**, 923-930, doi:10.1093/bioinformatics/btt656 (2014).

68   DeLuca, D. S. *et al.* RNA-SeQC: RNA-seq metrics for quality control and process optimization. *Bioinformatics* **28**, 1530-1532, doi:10.1093/bioinformatics/bts196 (2012).

69   genefilter: methods for filtering genes from high-throughput experiments v. R package version 1.76.0 (2021).

70   Love, M. I., Huber, W. & Anders, S. Moderated estimation of fold change and dispersion for RNA-seq data with DESeq2. *Genome Biol* **15**, 550, doi:10.1186/s13059-014-0550-8 (2014).

71   Ritchie, M. E. *et al.* limma powers differential expression analyses for RNA-sequencing and microarray studies. *Nucleic Acids Res* **43**, e47, doi:10.1093/nar/gkv007 (2015).

72   Davenport, E. E. *et al.* Genomic landscape of the individual host response and outcomes in sepsis: a prospective cohort study. *Lancet Respir Med* **4**, 259-271, doi:10.1016/S2213-2600(16)00046-1 (2016).

73   Pena, O. M., Pistolic, J., Raj, D., Fjell, C. D. & Hancock, R. E. Endotoxin tolerance represents a distinctive state of alternative polarization (M2) in human mononuclear cells. *J Immunol* **186**, 7243-7254, doi:10.4049/jimmunol.1001952 (2011).

13

596   74   Dominguez-Villar, M., Baecher-Allan, C. M. & Hafler, D. A. Identification of T helper
597   type 1-like, Foxp3+ regulatory T cells in human autoimmune disease. *Nat Med* **17**, 673-
598   675, doi:10.1038/nm.2389 (2011).
599

Tables
601   Supplementary Table 1. Participant characteristics.
602   Supplementary Table 2. Percentage of cells per cluster in each study group.
603   Supplementary Table 3. Pathway enrichment of all differentially expressed genes from COVID-
604   19 vs. healthy monocytes.
605   Supplementary Table 4. Pathway enrichment of upregulated genes from COVID-19 vs. healthy
606   monocytes.
607   Supplementary Table 5. Pathway enrichment of downregulated genes from COVID-19 vs. healthy
608   monocytes.
609   Supplementary Table 6. Pathway enrichment of all differentially expressed genes from stimulated
610   COVID-19 vs. stimulated healthy monocytes.
611   Supplementary Table 7. Pathway enrichment of upregulated genes from stimulated COVID-19 vs.
612   stimulated healthy monocytes.
613   Supplementary Table 8. Pathway enrichment of downregulated genes from stimulated COVID-19
614   vs. stimulated healthy monocytes.
615

Figure legends
617

618   **Figure 1. Unique phenotype of COVID-19 monocytes**. **a**. tSNE plots obtained from a
619   concatenated sample consisting of PBMC from n=15 healthy individuals, n=15 mild and n=15
620   moderate COVID-19 patients. **b**. Box and whiskers plots summarizing the median gMFI of the
621   receptors analyzed. The box extends from the 25th to the 75th percentile and the whiskers are drawn
622   down to the 10th percentile and up to the 90th percentile. Points below and above the whiskers are
623   drawn as individual points (n=25 healthy, n=15 mild and n=17 moderate COVID-19 individuals).
624   **c**. tSNE plots depicting the cell clusters identified by Phenograph from the concatenated sample in
625   **a**. **d**. Pie charts show the fraction of cells within each identified cell cluster in each patient group.
626   **e**. Bars graph show the distribution (percentage) of cells from each patient group in each identified
627   cell cluster. **f**. Heatmap of the expression of receptors per cell cluster displayed as modified z-
628   scores using median values. **g** and **h**. Summary of expression of activating (**g**) and repressive (**h**)
629   histone marks in monocytes from healthy individuals (n=20), mild (n=15) and moderate (n=11)
630   COVID-19 patients. One-way ANOVA with Tukey's correction for multiple comparisons for **b**,
631   **g**, **h**. *P<0.05, **p<0.005, ***p<0.001, ****p<0.0001.
632

633   **Figure 2. Gene expression signature of COVID-19 monocytes *ex vivo*.** **a**. Principal component
634   analysis (PCA) of the gene expression data computed from all genes from *ex vivo* healthy
635   individual (white dots) and moderate COVID-19 (blue dots) monocyte samples. PC2 plotted
636   against PC1 to explore overall variation across samples. The variance explained by each
637   component is stated in brackets. **b**. Volcano plot of differentially expressed genes for ex vivo
638   COVID-19 vs healthy monocytes. Red coloring shows genes with fold change ≥1.5 and
639   FDR<0.05. **c**. Bar plots depict significantly enriched (FDR<0.05) pathways from Reactome for
640   COVID-19 vs. healthy individual monocytes using upregulated genes in COVID-19 vs healthy
641   (≥1.5 fold increase, FDR<0.05), with the fold enrichment plotted on the x axis as $\log_2$ (FC) and

642 the bars labelled with the adjusted p value. **d**. Significantly upregulated genes in the COVID-19
643 vs healthy monocyte contrast that are members of the pathways in **c**, shown in a heatmap. Gene
644 expression values are scaled by row, with red indicating relatively high expression and blue low
645 expression. Both rows and columns are clustered using Euclidean distance and Ward's method. **e**.
646 Phospho-IRF3 (Ser 396) expression measured by flow cytometry and plotted as gMFI for healthy
647 (n=14), mild (n=15) and moderate (n=10) COVID19 monocytes. **f**. *IFITM2* relative gene
648 expression (to *GAPDH*) measured by real-time PCR in sorted CD14$^+$ monocytes from healthy
649 individuals (n=7), mild (n=7) and moderate (n=13) COVID-19. **g**. IκBα (left) and phospho-NFκB
650 p65 (right) expression measured by flow cytometry as gMFI in healthy individuals (n=14), mild
651 (n=15) and moderate (n=10) COVID-19 monocytes. **h**. Bar plots depict significantly enriched
652 (FDR<0.05) pathways from Reactome for COVID-19 vs. healthy individual monocytes, using
653 downregulated genes in COVID-19 vs. healthy (≥1.5 fold decrease, FDR<0.05), with the fold
654 enrichment plotted on the x axis as log$_2$ (FC) and the bars labelled with the adjusted p value. **i**.
655 Significantly downregulated genes in the COVID-19 vs. healthy monocyte contrast that are
656 members of the pathways in **h**, shown in a heatmap. Gene expression values are scaled by row,
657 with red indicating relatively high expression and blue low expression. Both rows and columns
658 are clustered using Euclidean distance and Ward's method. **j**. Representative example of *ex vivo*
659 expression of puromycin in CD14$^+$ monocytes measured by flow cytometry (left) and summary of
660 puromycin gMFI on healthy individuals (n=10), mild (n=8) and moderate (n=10) COVID-19
661 monocytes (right). **k**. Glycolytic capacity (left) and mitochondrial dependency (right) of
662 monocytes from healthy individuals (n=10), mild (n=8) and moderate (n=10) COVID-19
663 monocytes *ex vivo*. One-way ANOVA with Tukey's test for multiple comparisons in **e**, **f**, **g**, **j**, **k**.
664 *p<0.05, **p<0.005.
665
666 **Figure 3. Impaired *ex vivo* pathogen sensing by COVID-19 monocytes**. **a**. Representative
667 example of the production of TNF and IL-10 by CD14$^+$ monocytes from healthy individuals, mild
668 and moderate COVID-19 patients after *ex vivo* stimulation with SARS-CoV-2. **b**. Summary of
669 percentage of TNF- and IL-10-producing CD14$^+$ from CD14$^+$ monocytes after SARS-CoV-2
670 stimulation in healthy individuals (n=19), mild (n=18) and moderate (n=19) COVID-19 patients.
671 **c**. Summary of percentage of TNF- and IL-10-producing CD14$^+$ from CD14$^+$ cells after stimulation
672 with a mixture of heat-inactivated common cold coronaviruses (CCCoV, left) or LPS (right) in
673 healthy individuals (n=12 for CCCoV and n=13 for LPS stimulation), mild (n=21 for CCCoV and
674 n=18 for LPS stimulation) and moderate (n=12 for CCCoV and n=19 for LPS stimulation)
675 COVID-19 patients. **d**. Representative histograms of CD40 expression by healthy individual, mild
676 and moderate COVID-19 monocytes stimulated with vehicle (grey histogram) or SARS-CoV-2
677 (orange histogram). Numbers represent percentage of CD40$^+$ monocytes relative to vehicle-
678 stimulated cells. **e**. Summary of percentage of CD40$^+$CD14$^+$ from CD14$^+$ cells after SARS-CoV-
679 2 stimulation in healthy individuals (n=20), mild (n=22) and moderate (n=16) COVID-19 patients.
680 **f**. Summary of percentage of CD40$^+$CD14$^+$ from CD14$^+$ cells after stimulation with a mixture of
681 heat-inactivated common cold coronaviruses (CCCoV, left) or LPS (right) in healthy individuals
682 (n=17 for CCCoV and n=14 for LPS stimulation), mild (n=18 for CCCoV and n=22 for LPS
683 stimulation) and moderate (n=13 for CCCoV and n=10 for LPS stimulation) COVID-19 patients.
684 **g**. Summary of HLA-DR (left), CD80 (middle) and CD86 (right) expression measured by flow
685 cytometry and plotted as gMFI of CD14$^+$ monocytes from healthy individuals (n=15), mild (n=22)
686 and moderate (n=9) COVID-19 patients stimulated with vehicle (white dots) or SARS-CoV-2
687 (CoV2, orange dots). Lines link paired samples. **h**. Summary of H3K27Ac (left) and H3K4Me3

15

688 (right) expression measured by flow cytometry and plotted as gMFI of CD14$^+$ monocytes from
689 healthy individuals (n=20), mild (n=15) and moderate (n=11) COVID-19 patients stimulated with
690 vehicle (white dots) or SARS-CoV-2 (CoV2, orange dots). Lines link paired samples. **i**. Summary
691 of H3K27Me3 (left) and H3K9Me2 (right) expression measured by flow cytometry and plotted as
692 gMFI of CD14$^+$ monocytes from healthy individuals (n=20), mild (n=15) and moderate (n=11)
693 COVID-19 patients stimulated with vehicle (white dots) or SARS-CoV-2 (CoV2, orange dots).
694 Lines link paired samples. **j**. Energetic status measured by puromycin expression (gMFI) of
695 monocytes from healthy individuals (n=10), mild (n=8) or moderate (n=10) COVID-19 patients
696 stimulated with vehicle (open bars) or LPS (colored bars). **k**. Glycolytic capacity (%, left) and fatty
697 acid and amino acid oxidation capacity (%, right) of CD14$^+$ monocytes from healthy individuals
698 (n=10), mild (n=8) and moderate (n=10) COVID-19 patients stimulated with LPS. One-way
699 ANOVA with Tukey's correction for multiples comparisons in **b**, **c**, **e**, **f** and **k**. Two-way ANOVA
700 with Tukey's correction for multiple comparisons in **g**, **h**, **i**, **j**. *p<0.05, **p<0.005, ***p<0.001,
701 ****p<0.0001.
702
703 **Figure 4. Gene expression signature of COVID-19 monocytes upon pathogen sensing**. **a**.
704 Principal component analysis (PCA) of the gene expression data computed from all genes from
705 healthy individual (white dots) and moderate COVID-19 (blue dots) monocyte samples stimulated
706 with SARS-CoV-2. PC2 plotted against PC1 to explore overall variation across samples. The
707 variance explained by each component is stated in brackets. **b**. Volcano plots of differentially
708 expressed genes for activated COVID-19 vs. activated healthy monocytes. Red coloring shows
709 genes with fold change ≥1.5 and FDR<0.05. **c**. Bar plots depict the top 10 significantly enriched
710 (FDR<0.05) pathways from Reactome for COVID-19 vs. healthy individual monocytes stimulated
711 with SARS-CoV-2 using upregulated genes in COVID-19 vs healthy (≥1.5 fold increase,
712 FDR<0.05), with the fold enrichment plotted on the x axis as log$_2$ (FC) and the bars labelled with
713 the adjusted p value. **d**. Top 40 significantly upregulated genes in the COVID-19 vs healthy
714 monocyte contrast that are members of the pathways in **c**, shown in a heatmap. Gene expression
715 values are scaled by row, with red indicating relatively high expression and blue low expression.
716 Both rows and columns are clustered using Euclidean distance and Ward's method. **e**. Bar plots
717 depict the top 10 significantly enriched (FDR<0.05) pathways from Reactome for COVID-19 vs.
718 healthy individual SARS-CoV-2-stimulated monocytes, using downregulated genes in COVID-19
719 vs healthy (≥1.5 fold decrease, FDR<0.05), with the fold enrichment plotted on the x axis as log$_2$
720 (FC) and the bars labelled with the adjusted p value. **f**. Top 40 significantly downregulated genes
721 in the SARS-CoV-2-stimulated COVID-19 vs. healthy individual monocyte contrast that are
722 members of the pathways in **e**, shown in a heatmap. Gene expression values are scaled by row,
723 with red indicating relatively high expression and blue low expression. Both rows and columns
724 are clustered using Euclidean distance and Ward's method. **g**. Phospho-IRF3 (Ser 396) expression
725 measured by flow cytometry and plotted as fold change to baseline (gMFI) for healthy (n=14,
726 white dots), mild (n=15, light blue dots) and moderate (n=10, dark blue dots) COVID-19
727 monocytes stimulated with LPS for 60 minutes. **h**. *IFITM2* relative gene expression (to *GAPDH*)
728 measured by real-time PCR in sorted CD14$^+$ monocytes from healthy individuals (n=14), mild
729 (n=7) and moderate (n=23) COVID-19 stimulated with SARS-CoV-2. **i**. Phospho-NFκB p65 (Ser
730 529) expression measured by flow cytometry and plotted as fold change to baseline (gMFI) for
731 healthy (n=14, white dots), mild (n=15, light blue dots) and moderate (n=10, dark blue dots)
732 COVID-19 monocytes stimulated with LPS for 60 minutes. Mixed model with Tukey's post-test
733 for multiple comparisons for **g** and **i**. One-way ANOVA with Tukey's test for multiple

16

734 comparisons in **h**. For **g** and **i**, statistical significance of only baseline vs. other time points within
735 the same patient groups are shown. *p<0.05, ***p<0.001 for healthy individual comparisons,
736 #p<0.05, ##p<0.005 for mild COVID-19 patient comparisons, $$$p<0.001 for moderate COVID-
737 19 patient comparisons. ****p<0.0001.
738
739 **Figure 5. Endotoxin-induced tolerance signature significantly enriched in COVID-19**
740 **monocytes**. **a**. Correlation plot of sepsis vs. healthy individual gene expression signature and *ex*
741 *vivo* COVID-19 vs. healthy individual monocyte gene expression signature. Each point represents
742 a gene detected in both the public sepsis dataset and our COVID-19 RNA-seq dataset. The log_2FC
743 between sepsis and healthy controls is plotted against the log_2FC for *ex vivo* COVID-19 monocytes
744 vs. healthy control monocytes, and the points are colored according to the significance and
745 direction of effect in the COVID-19 contrast (grey, not significant; red, significantly upregulated,
746 blue, significantly downregulated). **b**. Correlation plot of sepsis vs. healthy individual gene
747 expression signature and SARS-CoV-2-stimulated COVID-19 vs. healthy individual monocyte
748 gene expression signature. **c**. Correlation plot of endotoxin-induced tolerance gene signature and
749 *ex vivo* COVID-19 vs. healthy monocyte signature. Each point represents a gene detected in both
750 the endotoxin gene signature and our COVID-19 vs. healthy RNA-seq dataset. The log_2FC
751 between endotoxin tolerance and LPS-response is plotted against the log_2FC for *ex vivo* COVID-
752 19 vs. healthy monocytes, and the points colored according to the significance and direction of
753 effect in the COVID-19 contrast. Some of the most differentially expressed genes in the COVID-
754 19 vs. healthy monocyte dataset are identified in the plot. **d**. Correlation plot of endotoxin-induced
755 tolerance gene signature and SARS-CoV-2-stimulated COVID-19 vs. healthy monocyte signature.
756 Each point represents a gene detected in both the endotoxin gene signature and our COVID-19 vs.
757 healthy RNA-seq dataset. The log_2FC between endotoxin tolerance and LPS-response is plotted
758 against the log_2FC for SARS-CoV-2-stimulated COVID-19 vs healthy monocytes, and the points
759 colored according to the significance and direction of effect in the COVID-19 contrast. Some of
760 the most differentially expressed genes in the COVID-19 vs. healthy monocyte dataset are
761 identified in the plot. **e**. Barcode plot showing enrichment of the endotoxin tolerance gene set (ET)
762 in the differential gene expression results for SARS-CoV-2-stimulated COVID-19 vs healthy
763 monocytes. The ranked test statistics from DESeq2 for the SARS-CoV-2-stimulated COVID-19
764 vs. healthy contrast are represented by the central shaded bar, with genes downregulated in
765 COVID-19 on the left and upregulated genes on the right. The ranks of the endotoxin tolerance
766 gene set within the COVID-19 contrast are indicated by the vertical lines in the central bar. The
767 weights of the endotoxin tolerance genes (log_2 (FC) from the ET differential expression analysis)
768 are indicated by the height of the red and blue lines above and below the central bar. The red and
769 blue lines at the top and bottom indicate relative enrichment of the endotoxin tolerance genes (split
770 into genes with positive and negative FCs in the ET contrast) in each part of the plot.
771
772 **Supplementary Figure 1. Number of cells per cluster identified by Phenograph.**
773
774 **Supplementary Figure 2. PCA gene loadings for RNA-seq of *ex vivo* isolated CD14+**
775 **monocytes from healthy individuals and moderate COVID-19 patients**. The features
776 contributing most to PC1 and PC2 (both positively and negatively) were identified using gene
777 loadings, and the top 10 features for each PC are indicated, with arrows drawn from the origin
778 illustrating their relative weights.

779 **Supplementary Figure 3. Pathway enrichment of COVID-19 monocyte RNA-seq data.**
780 Significantly enriched (FDR <0.05) pathways from Reactome for the *ex vivo* COVID-19 *vs.*
781 healthy control monocytes differentially expressed genes are displayed as a bar plot, with the fold
782 enrichment plotted on the x axis (log2(FC)) and the bars labelled with the adjusted p value.

784 **Supplementary Figure 4. Seahorse analysis of COVID-19 monocytes *ex vivo*.** Basal
785 extracellular acidification rate (ECAR, left) and basal oxygen consumption rate (OCR, right) were
786 measured in sorted CD14+ monocytes from healthy individuals (n=5) and COVID-19 patients
787 (n=5). **p<0.005 by paired t-test.

789 **Supplementary Figure 5. *Ex vivo* monocyte glucose metabolism and mitochondrial oxidation**
790 **dependency**. Glucose dependency (left) and mitochondrial oxidation dependency (right)
791 calculated using SCENITH^{TM} in healthy individuals (n=10, white bar), mild (n=8, light blue bar)
792 and moderate (n=10, dark blue bar) COVID-19 monocytes.

794 **Supplementary Figure 6. Seahorse analysis of activated COVID-19 monocytes**. Extracellular
795 acidification rate (ECAR, left) and oxygen consumption rate (OCR, right) were measured in sorted
796 CD14$^+$ monocytes from healthy individuals (n=5) and COVID-19 patients (n=5) stimulated or not
797 with 100 ng/ml LPS for 18 hours. ECAR and OCR shown as fold increase relative to unstimulated
798 controls **p<0.005 by paired t-test.

800 **Supplementary Figure 7. PCA gene loadings for RNA-seq of SARS-CoV-2-stimulated CD14$^+$**
801 **monocytes from healthy individuals and moderate COVID-19 patients**. The features
802 contributing most to PC1 and PC2 (both positively and negatively) were identified using gene
803 loadings, and the top 10 features for each PC are indicated, with arrows drawn from the origin
804 illustrating their relative weights.

806 **Supplementary Figure 8. Pathway enrichment of SARS-CoV-2-stimulated COVID-19**
807 **monocyte RNA-seq data.** Significantly enriched (FDR <0.05) pathways from Reactome for
808 SARS-CoV-2 COVID-19 *vs.* healthy control monocytes differentially expressed genes are
809 displayed as a bar plot, with the fold enrichment plotted on the x axis (log2(FC)) and the bars
810 labelled with the adjusted p value.

812 **Materials and Methods.**

814 *Participants and clinical data collection.*
815 Disease severity was categorized based on the WHO ordinal classification of clinical
816 improvement, where 0 (uninfected) describes people with no clinical or virological evidence of
817 infection, 1-2 describe ambulatory patients without (1) or with (2) limitation of activities, and 3-4
818 corresponds to hospitalized patients with no oxygen therapy (3) or oxygen by mask or nasal prongs
819 (4). Peripheral blood was collected from all participants and processed following a common
820 standard operating protocol. For inpatients, clinical data were abstracted from the electronic
821 medical records into summary participant sheets. Participant group characteristics are summarized
822 in Supplementary Table 1.

18

823 Healthy donors (WHO 0) were Imperial College staff with no prior diagnosis of or recent
824 symptoms consistent with COVID-19, and where possible, were matched in age and sex
825 distribution with COVID-19 patients.
826
827 Blood samples from the COVID-19 patients examined in this work come from two different
828 studies. COVIDITY study is a prospective observational serial sampling study of whole blood to
829 observe the evolution of SARS-CoV-2 infection to characterize the host response to infection over
830 time in peripheral blood (ethics approval obtained from the Health Research Authority, South
831 Central Oxford C Research Ethics Committee). The population of study were >18 year old patients
832 and/or staff at Imperial College Healthcare NHS Trust/Imperial College London with confirmed
833 COVID-19 from a positive SARS-CoV-2 RT-PCR testing from NHS laboratories or Public Health
834 England. Samples were taken 3-14 days after symptom initiation and were classified as 1 or 2
835 disease severity.
836
837 Samples from patients with moderate COVID-19 admitted to hospitals in London (Hammersmith
838 Hospital, Charing Cross Hospital, Saint Mary's Hospital) and eligible to participate in the MATIS
839 trial[61] provided consent (ethics approval by the Health Research Authority, London-Surrey
840 Borders Research Ethics Committee) and blood was collected 3-14 days after disease onset and 0-
841 2 days after hospitalization and positive PCR, and before study treatment initiation. Moderate
842 patients displayed mild of moderate COVID-19 pneumonia, defined as grade 3 or 4 WHO severity.
843 Samples were collected from March 2020 to February 2021 and none of the participants had
844 received a COVID-19 vaccine.
845
846 ***Cell Isolation and storage***.
847 Peripheral blood mononuclear cells (PBMCs) were isolated by Ficoll Hypaque (GE Healthcare)
848 gradient centrifugation <4 hours after blood collection. The PBMC layer was collected, washed
849 with PBS, resuspended at 20 million cells/ml in fetal bovine serum supplemented with 10% DMSO
850 and stored at -150 ºC or liquid nitrogen.
851
852 ***Flow cytometry stainings***.
853
854 PBMCs were thawed and rested for 2 hours at 37 ºC in RPMI 1640 media supplemented with 2
855 mM L-glutamine, 5% human AB serum, and 1x Penicillin and Streptomycin. For *ex vivo*
856 phenotypic characterization, 300,000-500,000 PBMC were stained with LIVE/DEAD Fixable
857 Dead Cell Dyes (Thermo Fisher Scientific) according to the manufacturer's specifications. A Fc
858 receptor (FcR) blocking step was performed using FcR Blocking Reagent Human (Miltenyi
859 Biotec) before cell surface antibody staining. The antibodies used in the stainings were the
860 following: CD14 (61D3, eBioscience), CD3 (UCHT1, BD), CD19 (HIB19, BD), CD1c (L161,
861 Biolegend), CD40 (5C3, Biolegend), CD141 (M80, Biolegend), CD304 (12C2, Biolegend), CD86
862 (BU63, Biolegend), CD80 (BB1, BD Pharmigen), HLA-DR (L243, Biolegend), CD301 (H037G3,
863 Biolegend), HLA-ABC (W6/32, Biolegend), TIM-3 (F38-2E2, Invitrogen), PD-1 (EH12.2H7,
864 Biolegend), and CD16 (3G8, BD). Cells were subsequently fixed using the Foxp3 staining buffer
865 kit (Thermo Fisher Scientific) following the manufacturer's recommendations and resuspended in
866 250 ul of PBS.
867

19

868 For intracellular staining, the abovementioned protocol was used and an additional step for
869 intracellular staining was added after fixation. The antibodies used for intracellular staining were
870 the following: H3K27Ac, H3K9Me2, H3K4Me3, H3K27Me3 (all from Cell Signaling
871 Technology), TNF (Mab11, Biolegen) and IL-10 (JES3-907, Thermo Fisher Scientific).
872 Intracellular staining was performed using the the Foxp3 staining buffer kit.

874 Samples were run on a Fortessa instrument (BD Biosciences) and analyzed using FlowJo v.10.
875 Dimensionality reduction and tSNE plots were obtained by downsampling each of the 15 samples
876 per group (healthy, mild COVID-19 and moderate COVID-19) to 1,500 events per sample, and
877 the concatenated sample was used to calculate tSNE axes using 1,000 iterations, perplexity of 40
878 and the default learning rate (4734). In order to obtain cell clusters, we used Phenograph[62] plugin
879 in FlowJo, with k=166 and all compensated parameters.

881 *Generation of virus stocks*.

883 SARS-CoV-2 virus (SARS-CoV-2/England/IC19/2020 isolate, kindly provided by Wendy S
884 Barclay) was expanded in Vero-E6 cells. Briefly, Vero-E6 cells were plated in serum-free medium
885 (OptiPRO SFM containing 2x GlutaMAX) in T75 flasks and infected with SARS-CoV-2 at a
886 multiplicity of infection of 0.1 and a final volume of 5 ml. Cells were incubated for 2 hours at 37
887 °C, 5% CO_2, after which the inoculum was removed and complete medium without serum was
888 added to the culture. Cells were incubated for 3-5 days (until cytopathic effects were observed).
889 Subsequently, cell culture supernatant was collected, centrifuged at 1000 x*g*, 4 °C for 15 minutes
890 and transferred to a new 50 ml tube for a second centrifugation at 1000 x*g*, 4 °C for 15 minutes.
891 Viral supernatant was collected, filtered through 0.45 μm and an aliquot was taken for titration.
892 The rest of the supernatant was UV-inactivated and concentrated using Retro-X concentrator
893 (Takara Bio), following manufacturer's recommendations and published protocols[63,64].

895 Human coronaviruses (CCCoV) 229E, OC43 and NL63 strains (Public Health England) were
896 expanded in MRC-5 (kindly provided by Dr Rob White, Imperial College London), BSC-1 (Public
897 Health England) and LLCMK2 (Public Health England), respectively. Briefly, cell lines were
898 plated in serum-free medium (DMEM, 1x non-essential amino acids) in T75 flasks and infected
899 with CCCoV (229E, OC43 or NL63) at a multiplicity of infection of 0.1 and a final volume of 5
900 ml. Cells were incubated for 2 hours at 37 °C, 5% CO_2, after which the inoculum was removed
901 and medium without serum was added to the culture. Cells were incubated for 3-5 days (until
902 cytopathic effects were observed). Subsequently, cell culture supernatant was collected,
903 centrifuged at 1000 x*g*, 4 °C for 15 minutes and transferred to a new 50 ml tube for a second
904 centrifugation at 1000 x*g*, 4 °C for 15 minutes. Viral supernatant was collected, filtered through
905 0.45 μm and an aliquot was taken for titration. The rest of the supernatant was heat-inactivated
906 and concentrated using Retro-X concentrator (Takara Bio), following manufacturer's
907 recommendations and published protocols[63,64].

909 *Titration of virus stocks.*
910 For SARS-CoV-2 titration, samples were serially diluted in OptiPRO SFM, 2X GlutaMAX (1:10)
911 and added to Vero cell monolayers for 1 hour at 37 °C, 5% CO_2. The inoculum was subsequently
912 removed and cells were overlayed with DMEM containing 0.2% w/v bovine serum albumin,
913 0.16% w/v $NaHCO_3$, 10 mM HEPES, 2 mM L-Gutamine, 1X P/S and 0.6% w/v agarose. Plates

914   were incubated at 37 °C, 5% CO_2 for 3 days. The overlay was then removed and monolayers were
915   stained with crystal violet solution for 1 hour at room temperature. Plates were washed with water,
916   dried and virus plaques were counted.

917

918   For CCCoV titration, viral supernatants were serially diluted in DMEM, non essential amino acids
919   (1:10) and added to MRC-5 (229E strain), BSC-1 (OC43 strain) or LLCMK2 (NL63 strain) cell
920   monolayers for 1 hour at 37 °C, 5% CO_2. The inoculum was subsequently removed and cells were
921   overlayed with DMEM medium for 4-5 days (until cytopathic effects were observed). An endpoint
922   dilution assay was used to determine viral infectivity titers[63].

923

924   ***Ex vivo stimulation assays.***
925   PBMC were thawed and rested for 2 hours at 37 ºC in complete media. 250,000 PBMC were plated
926   in polysterene plates (Corning) to prevent unspecific stimulation of monocytes by adherence to the
927   plastic plate[65]. Cells were stimulated with vehicle, UV-inactivated SARS-CoV-2 (CoV-2), 100
928   ng/ml LPS or a mixture of heat-inactivated common cold coronaviruses consisting of the 229E,
929   OC43 and NL63 strains (CCCoV) at 10^6 viral particles per 10^6 cells for 20 hours. For intracellular
930   stainings, GolgiStop[TM] (BD Biosciences) was added to the cultures 10 hours after stimulation for
931   a total of 10 hours.

932

933   ***RNA isolation, RNA quality control, and sample preparation for RNA-seq analysis.***
934   Sorted CD14^{+} monocytes from total PBMC either *ex vivo* or after a 20 hour stimulation with 10^6
935   UV-inactivated SARS-CoV-2 viral particles per 10^6 cells were lysed with RLT Plus buffer
936   (QIAGEN). RNA was isolated using the RNeasy Micro Plus Kit (QIAGEN) following the
937   manufacturer's guidelines in Appendix D of the QIAGEN RNeasy handbook. RNA quality was
938   quantified using the Agilent RNA 6000 Pico Kit (Agilent Technologies) following the
939   manufacturer's guidelines. RNA samples were stored at -80 °C until further processing.

940

941   ***RNA-seq analysis.***
942   RNA-sequencing was performed by the Oxford Genomics Centre. PolyA-enriched strand- specific
943   libraries were prepared using NEBNext Ultra II Directional RNA Library Prep Kits (Illumina). All
944   samples were pooled together and 150bp PE reads were sequenced on a Novaseq system, resulting
945   in a median read count of 28M per sample.

946

947   Raw data was processed using the Sanger Nextflow RNA-seq pipeline
948   . Briefly, reads were aligned to the reference genome (GRCh38.99) using
949   STAR v2.7.3[66] in the two-pass mode (ENCODE recommended parameters) and gene expression
950   was quantified using featureCounts[67]. Mapping statistics and quality control metrics from FastQC
951   and RNA-SeQC[68] indicated high data quality for all samples with no outliers detected.
952   RNA-seq data analysis was performed in R v4.1 in Rstudio Server. Features that did not have at
953   least 10 reads in at least 6 samples (the size of the smallest biological subgroup) were filtered out
954   using the genefilter package[69], resulting in a processed data set on 16,328 features. Principal
955   component analysis (PCA) with the prcomp function was used to explore the relationship between
956   samples, after the filtered gene counts were transformed using a regularized log transformation
957   from the DESeq2[70] package.

958

959 Differential gene expression analysis was carried out using DESeq2, comparing unstimulated
960 monocytes from COVID-19 patients (n=10) to unstimulated monocytes from healthy controls
961 (HC) (n=6), and SARS-CoV-2-stimulated monocytes from COVID-19 patients (n=14) to
962 stimulated monocytes from HC (n=12). Genes with FDR<0.05 and a fold change (FC)≥1.5 were
963 deemed significantly differentially expressed. Pathway enrichment analysis was performed using
964 Fisher's exact test in XGR[29] with annotations from Reactome, using all genes retained in the
965 processed RNA-seq data as the background, and employing the xEnrichConciser options. An
966 adjusted p-value (BH FDR) threshold of 0.05 was used to identify significantly enriched pathways.
967 Pheatmap package was used to draw heatmaps illustrating variation in gene expression across
968 samples.
969
970 For testing the enrichment of the sepsis signature in our datasets, publicly available microarray
971 gene expression data on sepsis patients and healthy controls were accessed using GEOquery
972 (GSE46955)[50]. Gene expression between patients and controls was compared using limma[71], for
973 both the unstimulated and stimulated conditions. Subsequently, the estimated fold changes were
974 tested for correlation with those from the COVID-19 vs HC results. Where multiple probes were
975 available for the same gene in the microarray dataset, the top ranked probe was selected for the
976 comparison.
977
978 For comparison to the endotoxin-induced tolerance signature, we have previously defined an
979 endotoxin tolerance gene signature[72] from publicly available microarray data on *in vitro* LPS-
980 stimulated monocytes. Briefly, two datasets (GSE15219[52] and GSE22248[73]) were accessed
981 through GEO. Genes that were differentially expressed following a single LPS treatment (LPS
982 response genes), and that were also differentially expressed between singly- and doubly-stimulated
983 cells were identified. This resulted in an endotoxin tolerance gene signature comprising 398 genes,
984 of which 318 were detected in the RNA-seq dataset. We tested for enrichment of this gene set in
985 the COVID-19 versus healthy contrasts using the geneSetTest function and barcodeplot functions
986 from limma.
987
988 ***Quantification of mRNA expression by RT-PCR.***
989 Isolated RNA was converted to complementary DNA by reverse transcription (RT) with random
990 hexamers and Multiscribe RT (TaqMan Reverse Transcription Reagents; Thermo Fisher
991 Scientific). For *IFITM2* expression assays, the Hs00829485_sH probe was used from Thermo
992 Fisher Scientific. The reactions were set up using the manufacturer's guidelines and run on a
993 StepOnePlue Real-Time PCR Machine (Thermo Fisher Scientific). Values are represented as the
994 difference in cycle threshold (Ct) values normalised to *GAPDH* expression (Hs02786624_g1) for
995 each sample as per the following formula: Relative RNA expression = (2-ΔCt) x 1000[74].
996
997 ***Metabolic profiling using SCENITH^{TM}.***
998 SCENITH^{TM} is a flow cytometry-based method for profiling energy metabolism with single cell
999 resolution[35] *ex vivo* or after *in vitro* stimulation in sorted cells or complex cell mixtures. It uses
1000 puromycin incorporation to nascent proteins as a measurement for protein translation, which is
1001 tightly coupled to ATP production and therefore can be used as a readout for the energetic status
1002 of the cells at a given time.
1003

1004 PBMC were plated at 250,000-300,000 cells per well in 96 well plates and rested for 2 hours at 37
1005 °C, 5% CO_2 for *ex vivo* stainings, or rested for 2 hours and stimulated for 20 hours with 100 ng/ml
1006 LPS. Subsequently, cells were treated for 45 minutes at 37 °C, 5% CO_2 with Control (vehicle, Co),
1007 100 mM 2-deoxy-D-glucose (DG, Sigma-Aldrich), 1 μM oligomycin (O, Sigma-Aldrich) or a
1008 combination of both drugs (DGO). 10 μg/ml puromycin was added to all conditions for the same
1009 amount of time. Cells were subsequently washed with room temperature PBS and stained for
1010 viability, cell surface markers and fixed as described above. Intracellular staining of puromycin
1011 was performed using the anti-puromycin monoclonal antibody (1:600 dilution, clone R4743L-E8)
1012 for 45 minutes at 4 °C. The anti-puromycin antibody and metabolic inhibitors for SCENITH^{TM}
1013 were kindly provided by Dr Argüello.

1014
1015 For the analysis of the energetic status of cells, puromycin geometric mean fluorescence intensity
1016 was analyzed in each of the four abovementioned conditions (Co, DG, O, DGO). To calculate the
1017 percentage of glucose dependence, the following formula was used: 100*((Co-DG)/(Co-DGO).
1018 Mitochondrial dependence (%) was calculated as 100*((Co-O)/(Co-DGO). Glycolytic capacity
1019 (%) was calculated as 100-Mitochondrial dependence. Fatty acid and amino acid oxidation
1020 capacity (%) was calculated as 100-Glucose dependence.

1021
1022 ***Metabolic profiling using Seahorse.***
1023 Sorted CD14$^+$ monocytes from unstimulated or SARS-CoV-2-stimulated (20 hours at 37 °C, 5%
1024 CO_2) PBMC were plated at a range of 80,000-120,000 in duplicates for healthy and COVID-19
1025 sample pairs, based on the minimum cell number obtained for each pair of samples in individual
1026 experiments. An XFp real-time ATP rate assay kit (Agilent Technologies) was used following
1027 manufacturer's recommendations and samples were run in a Seahorse XF HS Mini Analyzer
1028 (Agilent Technologies). For basal oxygen consumption rate (OCR) and extracellular acidification
1029 rate (ECAR) measurements, 10 cycles were run and their average was taken as basal values per
1030 subject tested.

1031
1032 ***Phosphorylation assays by flow cytometry***.
1033 For *ex vivo* phosphorylation assays, thawed PBMC were plated at 250,000 cells per well in 96 well
1034 polypropylene plates and rested for 2 hours at 37 °C, 5% CO_2. PBMC were fixed with pre-warmed
1035 (37 °C) Cytofix (BD Biosciences) for 20 minutes at 37 °C, 5% CO_2 and permeabilized with Perm
1036 III buffer (BD Biosciences) overnight at -20 °C. Cultures were subsequently stained with CD3
1037 (UCHT1, BD Biosciences), CD20 (H1, BD Biosciences), CD14 (M5E2, Biolegend), CD16
1038 (B73.1, BD Biosciences), phospho-IRF3 (Ser 396, Bioss), phospho-NFkB p65 (Ser 529, BD
1039 Biosciences) in PBS for 1 hour at room temperature, washed with PBS and resuspended in 250 μl
1040 PBS.

1041
1042 For phosphorylation assays after LPS stimulation, PBMC were plated as above and stimulated
1043 with 100 ng/ml LPS for a total of 1 hour. Samples were fixed at 0, 5, 15, 30, 45 and 60 minutes
1044 after LPS addition for 20 min at 37 °C, 5% CO_2 and stained as above.

1045
1046 **Acknowledgements**.

23

Author contributions.

AKM performed experiments, analyzed data and wrote the manuscript, KLB analyzed the RNA-seq data and wrote the manuscript, EJ performed experiments, LB prepared SARS-CoV-2 virus stocks, CS and NG performed experiments, CES and RQ provided patient samples, RA provided the SCENITH^{TM} kit reagents and advised on SCENITH^{TM} data analysis and interpretation, WSB provided SARS-CoV-2 virus stock, NC provided patient samples and advised on the clinical aspects of COVID-19, GPT provided COVID-19 patient samples and advised on the clinical aspects of COVID-19, EED supervised RNA-seq data analysis and wrote the manuscript, MDV designed the study, performed experiments, analyzed data, wrote the manuscript and obtained funding. All authors revised and contributed to the editing of the manuscript.

Competing interest declaration

The authors declare no competing interests to declare.

Data availability.

RNA-seq data will be available at the European Genome-Phenome Archive (EGA) upon manuscript acceptance.

Additional information.
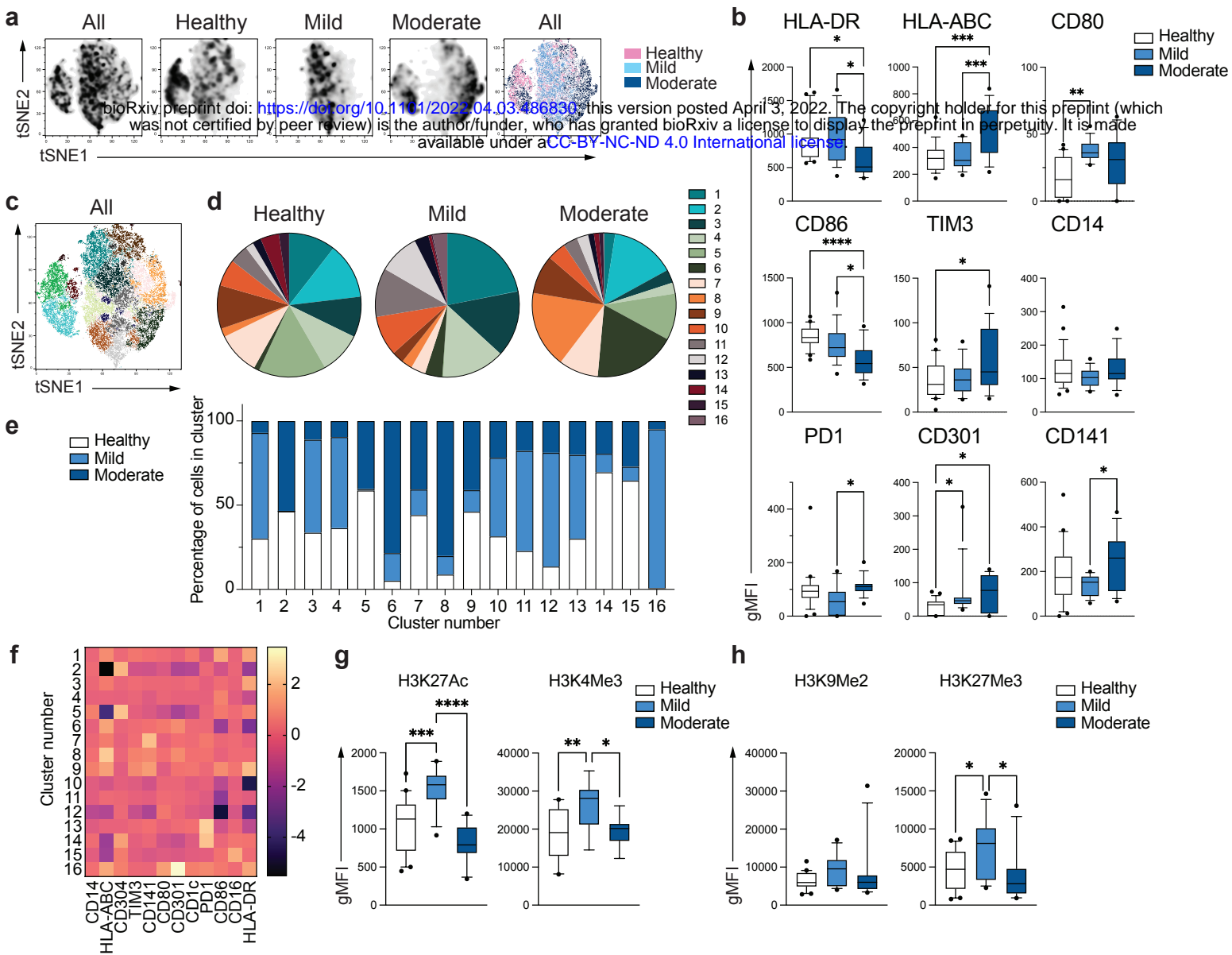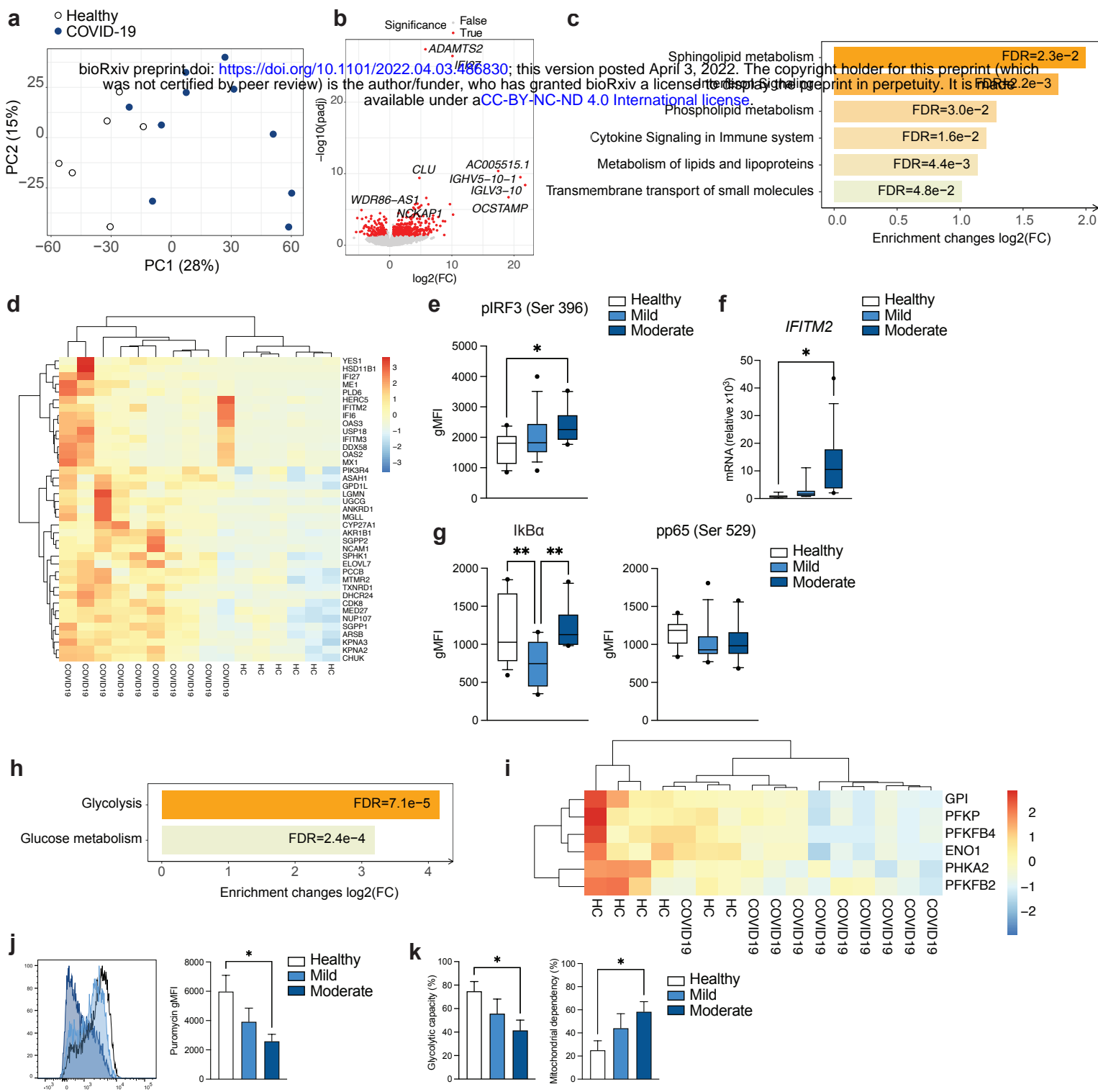
Corresponding author: Margarita Dominguez-Villar, m.dominguez-villar@imperial.ac.uk
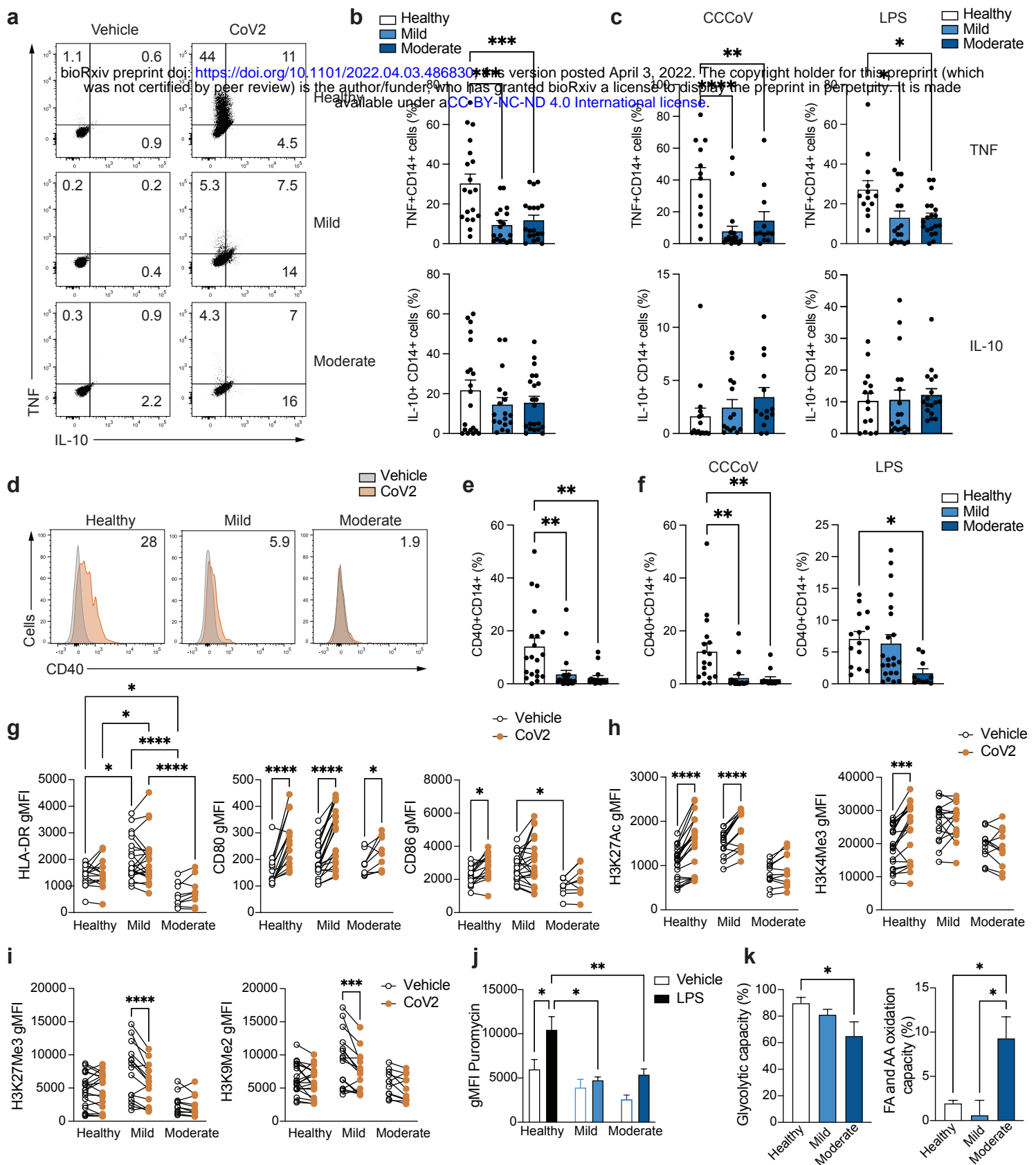
Figure 1

Figure 2

Figure 3

Figure 4

Figure 5

Supplementary Figure 1

Supplementary Figure 2

Supplementary Figure 3.

Supplementary Figure 4

Supplementary Figure 5

Supplementary Figure 6

Supplementary Figure 7

Supplementary Figure 8